



**UNIVERSITY OF LEEDS**

This is a repository copy of *A nutrient control on marine anoxia during the end-Permian mass extinction*.

White Rose Research Online URL for this paper:  
<http://eprints.whiterose.ac.uk/163093/>

Version: Supplemental Material

---

**Article:**

Schobben, M, Foster, WJ, Sleveland, ARN et al. (8 more authors) (2020) A nutrient control on marine anoxia during the end-Permian mass extinction. *Nature Geoscience*, 13. pp. 640-646. ISSN 1752-0894

<https://doi.org/10.1038/s41561-020-0622-1>

---

**Reuse**

Items deposited in White Rose Research Online are protected by copyright, with all rights reserved unless indicated otherwise. They may be downloaded and/or printed for private study, or other acts as permitted by national copyright laws. The publisher or other rights holders may allow further reproduction and re-use of the full text version. This is indicated by the licence information on the White Rose Research Online record for the item.

**Takedown**

If you consider content in White Rose Research Online to be in breach of UK law, please notify us by emailing [eprints@whiterose.ac.uk](mailto:eprints@whiterose.ac.uk) including the URL of the record and the reason for the withdrawal request.



[eprints@whiterose.ac.uk](mailto:eprints@whiterose.ac.uk)  
<https://eprints.whiterose.ac.uk/>

# **A nutrient control on marine anoxia during the end-Permian mass extinction**

## **Supplementary Information file**

Martin Schobben<sup>1,2</sup>, William J. Foster<sup>2,3</sup>, Arve R.N. Sleveland<sup>4</sup>, Valentin Zuchuat<sup>4</sup>, Henrik H. Svensen<sup>4</sup>, Sverre Planke<sup>4</sup>, David P.G. Bond<sup>5</sup>, Fons Marcelis<sup>6</sup>, Robert J. Newton<sup>1</sup>, Paul B. Wignall<sup>1</sup>, Simon W. Poulton<sup>1</sup>

---

<sup>1</sup> School of Earth and Environment, University of Leeds, Leeds, LS2 9JT, UK

<sup>2</sup> Museum für Naturkunde, Leibniz Institute for Research on Evolution and Biodiversity, 10115 Berlin, Germany

<sup>3</sup> Universität Potsdam, Institute of Geosciences, Potsdam, Germany

<sup>4</sup> Centre for Earth Evolution and Dynamics (CEED), Department of Earth Sciences, University of Oslo, P.O. box 1028, Blindern, 0315 Oslo, Norway

<sup>5</sup> School of Environmental Sciences, University of Hull, Hull, HU6 7RX, UK

<sup>6</sup> Shell Global Solutions International B.V., Postbus 38000, 1030 BN Amsterdam, Netherlands

This supplementary information files contains additional information on the applied methods and data quality; and additional discussion on the fidelity of the geochemical signals as well as extensive descriptions of the study sites in terms of lithology, stratigraphy and palaeontology. Data as well as the R Markdown scripts for data processing, statistics and visualization are provided along with this document (on Zenodo: <https://doi.org/10.5281/zenodo.3878094>).

## 1 Geological setting

The Svalbard island group is situated between 74 and 81 °N on the northwestern part of the Barents Shelf (Fig. 1). During Permian time the area was part of an extensive shelf on the northwestern margin of Pangaea situated at a palaeolatitude of ~40–45 °N (Supplementary Fig. 1 and ref 1). A fold-and-thrust belt, ranging over more than 300 km, exposes Palaeozoic, Mesozoic and Cenozoic strata along the west coast of the main island (Spitsbergen) from the Brøgger peninsula in the North to the Sørkapp in the southernmost tip. The Festningen site (78.09 °N, 13.88°E) on the southern entrance of the Isfjorden (Western Nordenskiöld Land) is an easily accessible and frequently studied stratigraphic profile. At this site strata dips at a ~45 ° angle in a eastward direction as part of the short limb of a NNW–SSE-striking asymmetric syncline<sup>2,3</sup>. The coastal cliffs of the Festningen site extend in an E-W direction providing an easy accessible opportunity to traverse the strata. A second P–Tr stratigraphic sequence at Deltadalen (78.27 °N, 16.88 °E) was drilled south of the coast of the Sassenfjorden/Tempelfjorden<sup>4</sup>. Here Permian and Triassic strata are relatively flat-lying with only minor folds and thrusts<sup>5</sup>.

Permian–Triassic (251.9 Mya)

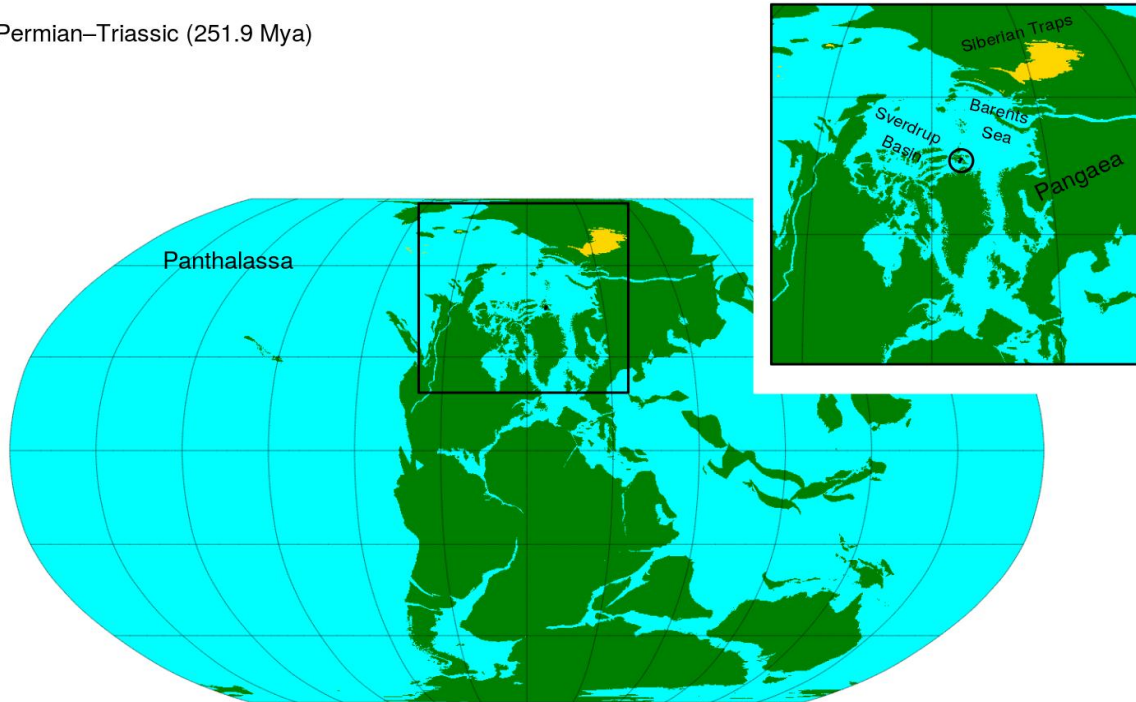


**Figure 1: Palaeogeographic reconstruction including the location of the sampled localities (circle in inset) and the Siberian Traps Basalts (yellow area, after ref. 6). Reconstruction with GPlates (<https://www.gplates.org>) and after refs. 7 and 8.**

## **2 Lithostratigraphy and facies description**

The Kapp Starostin Formation<sup>1</sup> is dominated by biogenic cherts (spiculites) with subordinate cherty shales, brachiopod and bryozoan-rich limestones and glauconitic sandstones<sup>9,10</sup>. Although substantial differences between the lithologies of outer Isfjorden of western-most Spitsbergen (Festningen) and inner Isfjorden of central Spitsbergen (Deltadalen), which has led to the

proposal of two distinct members; the Hovtinden and Stensiöfjellet members<sup>1</sup>, respectively, these units grade laterally into each other (Supplementary Fig. 2)<sup>9</sup> and can therefore be correlated. These two lithologies are interpreted to record shallow marine, high energy conditions in the inner Isfjorden (Stensiöfjellet Member)<sup>4</sup> whilst dark shales and cherts dominated in more distal, deeper locations (Hovtinden Member) that occurred in the outer Isfjorden<sup>9,12</sup>. Our study section at Festningen comprises the most expanded development of the Kapp Starostin Formation and has relatively thin beds of limestone indicating its distal, deep water development compared to the more easterly Deltadalen site. This sand-rich site was probably part of the inner sandy shelf that developed in north and east Spitsbergen in the Permian (Fig. 1).

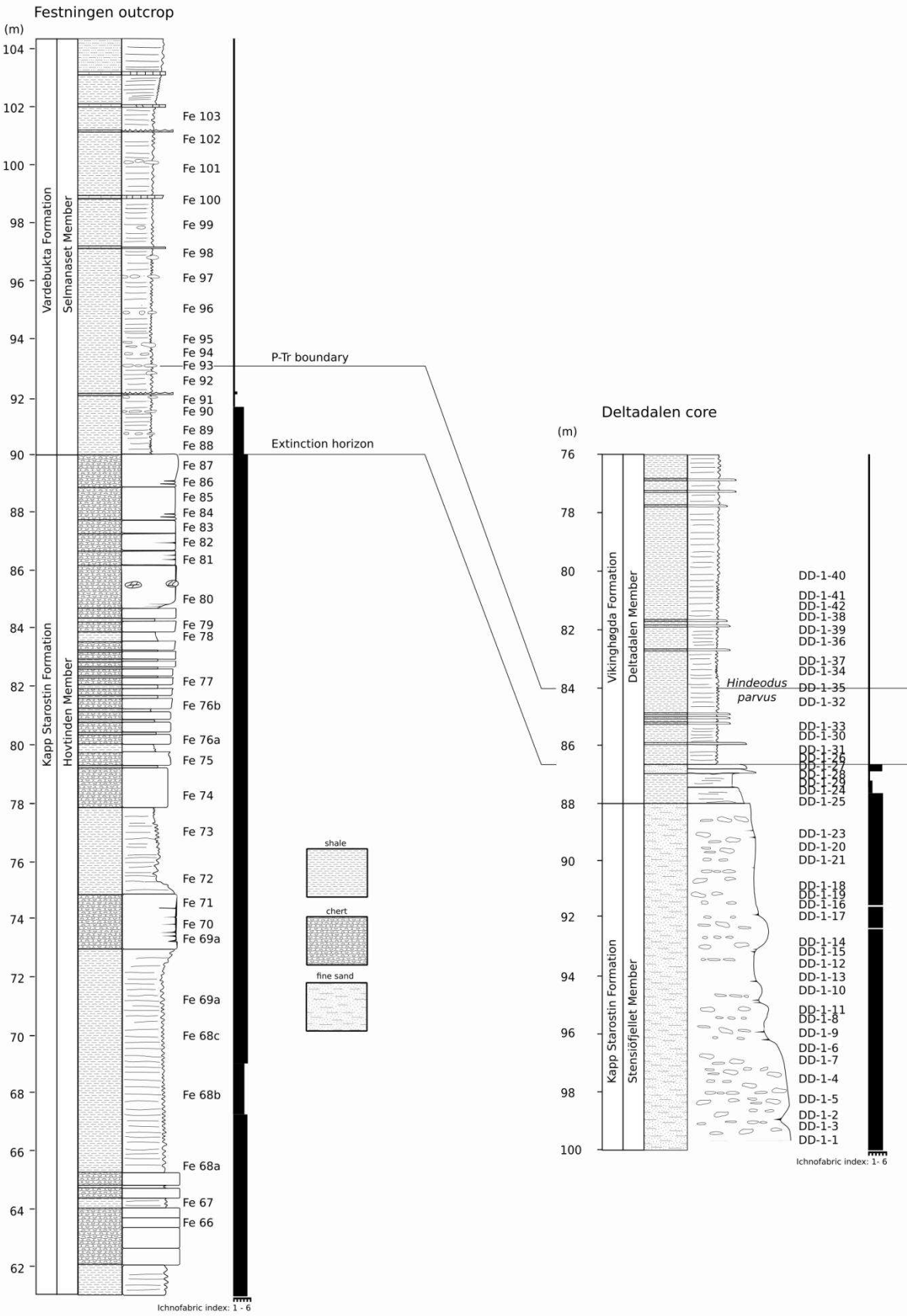


**Figure 2: Detailed lithology logs of the Deltadalen core and Festningen outcrop as well as a correlation scheme linking both sections.** Location of the Permian–Triassic for Deltadalen based on the first appearance datum of *Hindeodus parvus* after ref 4.

During the Early Triassic the west-to-east thinning of the stratigraphy persisted although the facies became dominated by fine-grained clastic material (of the Vardebukta<sup>13</sup> and Vikinghøgda<sup>5</sup> formations in the outer and inner Isfjorden, respectively) following the demise of siliceous sponges<sup>14,15</sup>. However, glauconitic sandstones persist 1.5 m above the the base of the Vikinghøgda Formation but the lithology is different from the underlying unit as it lacks diagenetic chert nodules (Supplementary Fig. 2)<sup>4,5,15,16</sup>. Although some signs of condensation exist in the upper meter of the Kapp Starostin Formation at Deltadalen, there are no erosive surfaces, and so no significant gaps are present in the studied sequences<sup>4,17</sup>. A stratigraphically confined, sharp shift to more <sup>13</sup>C-enriched C<sub>org</sub> (Fig. 2) might be interpreted as a sedimentary discontinuity. However, such shifts to higher  $\delta^{13}\text{C}_{\text{org}}$  might also be related to a change to more terrestrial derived C<sub>org</sub><sup>18</sup>, or a change in the predominant plankton communities that produced the organic matter<sup>19</sup>, where both scenarios would be parsimonious within the environmental context of elevated soil erosion and marine redox change (see main text).

The deposition of the here-studied units occurred in an open-marine shelf setting<sup>5</sup>. Initially, during the P–Tr boundary interval, deepest-water facies continued to be developed in the Festningen area. Progradation of sandy shoreface facies from a sediment source to the west saw shallower water conditions develop in western Spitsbergen in the Early Triassic<sup>4,14</sup>.

### 3 Chronology

The uppermost beds of the Kapp Starostin Formation are of Late Permian age, where the whole lithological unit (~380 m at Festningen) comprises a long time interval (Artinskian–Changhsingian), based on bryozoa, foraminifera, conodont, and brachiopod biostratigraphy as well as  $\delta^{13}\text{C}$  chemostratigraphy<sup>9,10,12,20</sup>. The abrupt lithological shift at the formation boundary has been interpreted as the die-off of a prolific silica producing metazoan community (sponges)(Supplementary Fig. 2), and also contains the disappearance of deep-tiered ichno fossil *Zoophycos*, which is synchronous with the global-scale biotic crisis<sup>17</sup>. Although faint signs of life persist in the form of bioturbation in the shale facies up to a height of ~3 m above the base of the Vardebukta Formation at Festningen (Supplementary Fig. 2), whereafter burrows disappear and sediments become finely laminated. A glauconitic sandstone unit, occurring above the base of the Vikinghøgda Formation (Supplementary Fig. 2) and contains a diverse ichno fabric assemblage (see Supplementary section 7.1.2) and, as such, the extinction horizon is placed above this unit<sup>15</sup>. Occurrences of the ammonite *Otoceras boreale* and species of the bivalve *Claraia*, 4–10 m above the base of the Vardebukta and Vikinghøgda formations are age-diagnostic fossils for the Griesbachian (earliest Triassic)<sup>2,4,5,17,21</sup>. Furthermore, at Deltadalen the marker conodont species *Hindeodus parvus* that defines the P–Tr boundary worldwide<sup>22</sup> has recently been uncovered<sup>4</sup>. Based on these considerations, a latest Permian age has been inferred for the shale and sandstone units above the formational boundary of Festningen and Deltadalen, respectively<sup>4,10,15–17</sup>. Carbon isotope based chemostratigraphy offers an alternative refined age control, where P–Tr event beds worldwide record a long-term negative  $\delta^{13}\text{C}$  anomaly that relates to a perturbation of the global biogeochemical carbon cycle<sup>23</sup>. Based on this premise, the  $\delta^{13}\text{C}_{\text{org}}$  minimum has been used as an alternative stratigraphic marker for P–Tr boundary sequence at

Festningen, which have so far not yielded the marker conodont species *H. parvus*<sup>3,24</sup>. Adopting this approach helped define the position of the P–Tr boundary in both sequences (Fig. 2 and Supplementary Fig. 2), and suggests that the successions record an age range of roughly Changhsingian to earliest Triassic.

## 4 Materials

The Festningen section was sampled at approximately one meter intervals during a sampling campaign in July 2012. The Deltadalen core was recovered during an expedition in 2014 and the core is currently deposited at the University of Oslo. Samples were taken at a 0.5 m resolution from the lowest 20 m of the core. The outcrop samples from Festningen were sawn in pieces and weathered surfaces were discarded along with material showing diagenetic textures. In turn, the samples were crushed manually and, depending on the samples size, either ground with a mechanical agate mill or an agate pestle and mortar.

## 5 Data processing, statistics and visualization

This work was generated with the aid of Rmarkdown (*knitr*)<sup>25–27</sup> on the programming platform R<sup>28</sup> and data processing and visualization was aided by the R packages: *tidyverse*<sup>29</sup>, *gtable*<sup>30</sup>, *png*<sup>31</sup>, *gridExtra*<sup>32</sup>, *readxl*<sup>33</sup>, *bibtex*<sup>34</sup>, *sp*<sup>35,36</sup>, *rgdal*<sup>37</sup>, *rgeos*<sup>38</sup>, *lattice*<sup>39</sup>, and *grid*<sup>28</sup>. The library *marelac*<sup>40</sup> was used for chemical data transformations.\*

---

\* R version 3.6.3 (2020-02-29), with: bibtex 0.4.2, grid 3.6.3, gridExtra 2.3, gtable 0.3.0, knitr 1.28, lattice 0.20-38, marelac 2.1.9, png 0.1-7, readxl 1.3.1, rgdal 1.4-6, rgeos 0.5-2, sp 1.3-1, tidyverse 1.2.1.

## 6 Methods

### 6.1 Sequential extractions and elemental analysis

Samples splits of ~100 mg were fully digested with a combination of 5 ml HNO<sub>3</sub>, 2 ml HF and few drops of HClO<sub>4</sub>. The acquired solutions were subsequently measured for their major and minor element contents by Inductively Coupled Plasma Optical Emission Spectrometry (ICP-OES; Thermo Scientific iCAP 7400 Radial) and Inductively Coupled Plasma Mass spectrometry (ICP-MS; Thermo Scientific iCAPQc), respectively. The solutions were spiked with an internal standard prior to the ICP analysis to correct for potential drift in the machine-internal analytical precision. Certified reference materials (USGS: SBC-1 and SGR-1) were measured along with the selected samples to monitor the external precision of the analytical procedure. Repeated analysis on the reference material confirms that values are reproducible to within 8% (relative standard deviation: RSD) and with a recovery of about 95% (and 109% for Mo and U) of the assigned value (Supplementary Table 1).

**Table 1: Summary statistics certified USGS reference material SBC-1 and SGR 1 for major and minor elements, respectively.**

phase	name	mean	SD	RSD (%)	n	assigned
Fe <sub>tot</sub>	SBC-1	6.47	0.22	3	51	6.79
	SGR 1b	2.00	0.12	6	3	2.12
Al	SBC-1	10.46	0.50	5	51	11.11
	SGR 1b	3.42	0.28	8	3	3.45
P <sub>tot</sub>	SBC-1	0.15	0.00	2	51	0.16
	SGR 1b	0.12	0.00	1	3	0.14

<b>Mo*</b>	<b>SGR 1b</b>	<b>38.73</b>	<b>0.11</b>	<b>0</b>	<b>3</b>	<b>35.00</b>
<b>U*</b>	<b>SGR 1b</b>	<b>5.08</b>	<b>0.04</b>	<b>1</b>	<b>3</b>	<b>4.70</b>
<b>Re**</b>	<b>SGR 1b</b>	<b>35.77</b>	<b>0.87</b>	<b>2</b>	<b>3</b>	<b>NA</b>

Mean, SD and published values are in wt. %, except for elements labelled with an \*, which are given in  $\mu\text{g/g}$ , and \*\*, which is given in  $\text{ng/g}$

In addition, sequential extraction procedures were applied to separate different sedimentary Fe and P phases. Firstly, the Fe speciation was used to reconstruct water column redox conditions, by combining sequential extractions, after ref. 41, with iron-sulfide extractions, by chromium-reducible sulfur (CRS), after ref. 42. Combined these methods yields six operationally-defined Fe fractions (Supplementary Table 2). Non-sulfidized iron was liberated during the sequential extraction scheme applied to a sample split of  $\sim 70$  mg, with solutions specifically targeting ferrous carbonates ( $\text{Fe}_{\text{carb}}$ ), Fe (oxyhydr)oxides ( $\text{Fe}_{\text{ox}}$ ; such as, ferrihydrite, lepidocrocite, goethite and hematite) and magnetite ( $\text{Fe}_{\text{mag}}$ ). A further iron reservoir (termed ‘poorly reactive Fe’; or  $\text{Fe}_{\text{PR}}$ ) was solubilized by boiling a sample split with 12 N HCl<sup>43</sup>. By subtracting  $\text{Fe}_{\text{HR}}$  (not including pyrite, which is not extracted by a boiling HCl extraction, after ref. 43) from  $\text{Fe}_{\text{PR}}$ , the fraction of iron contained in less reactive sheet silicate minerals (termed ‘poorly reactive sheet silicate Fe’; or  $\text{Fe}_{\text{PRS}}$ ) was obtained<sup>44,45</sup>. This iron phase is only poorly reactive to dissolved sulfide<sup>44</sup>, on a long timescale of  $10^5$ – $10^6$  y. However,  $\text{Fe}_{\text{HR}}$  is commonly transferred to the  $\text{Fe}_{\text{PRS}}$  pool during diagenesis under Fe reducing conditions in the absence of significant dissolved sulfide (see Supplementary Section 7.2 and the main text). The iron content of the various extractions was obtained by Atomic Absorption Spectrometry (AAS; Thermo Scientific, iCE 3000 Series). The CRS method solubilized metal sulfides (among which iron sulfides are by far the dominant contributor) from a sample split of 300–1500 mg. Pyritized Fe ( $\text{Fe}_{\text{py}}$ ) was derived

stoichiometrically from the weight of the liberated sulfide, captured as an Ag<sub>2</sub>S precipitate (Supplementary Table 2).

**Table 2: The successive steps of the sequential iron extraction; the respective extraction solutions and procedures, and the targeted operationally defined iron phases<sup>41</sup>.**

Step	Reagents	Fe-bearing phase
1-a	10 ml 1 M Na-acetate solution (pH 4.5, shake for 48 h at 50 °C)	Fe <sub>carb</sub> : iron bound to carbonate
1-b	10 ml Na-dithionite solution, citrate	Fe <sub>ox</sub> : iron bound to iron(oxyhydr)oxides
1-c	10 ml Ammonium oxalate solution (shake for 6 h)	Fe <sub>mag</sub> : iron bound as magnetite
2	5 ml 12 N HCl (boiling for 1 min)	Fe <sub>PR</sub> : iron bound to e.g. sheet silicates
3	ashing at 550 °C, 5 ml conc. HNO <sub>3</sub> , ~2 ml conc. HF (boiling and evaporating 120-150 °C to dryness)	Fe <sub>tot</sub> : total iron, including silicates
4	~16 ml CrCl <sub>2</sub> solution (boiling for 60 min, H <sub>2</sub> S driven out by bubbling with N <sub>2</sub> , precipitated in AgNO <sub>3</sub> trap)	Fe <sub>py</sub> : iron bound as CRS (pyrite)

To monitor the external reproducibility of the sequential Fe extraction procedure, several in-house reference materials were processed along with the sample material and replicate analyses generally yielded RSDs of < 9% (with the exception of phases which were at very low concentration). Pyrite Fe was determined with a RSD of 5%.

A modified version of the SEDEX protocol<sup>46,47</sup> was used to separate a sample split of ~150 mg into seven operationally defined phosphorus-bearing phases (Supplementary Table 3). The phosphorus content of the various phases was determined with a Thermo Scientific GENESYS 6 UV-Vis Spectrophotometer (880 nm) via the molybdate blue method<sup>46</sup>. Colour development after addition of molybdate blue is impaired in steps 1-a, 1-d and 1-e (Supplementary Table 3), and, as such, the P concentrations of these extractions were instead obtained by ICP-OES. For this, the

ICP-OES was used in radial mode with an argon humidifier attached to the nebuliser gas line. The argon humidifier helps to prevent blockages of the nebuliser caused by salt build up. In line with bulk-rock analysis, machine-internal precision was improved by the addition of an internal standard to the solutions. In line with the Fe sequential extraction, internal consistency for the individual extracts was checked by the additional processing of a set of in-house reference materials throughout the sequence. Repeated measurements of these reference values suggest that the values are reproducible to within 23% (RSD).

**Table 3: The successive steps of the sequential phosphorus extraction; the respective extraction solutions and procedures; the step-specific operationally defined phosphorus phase<sup>47</sup>.**

Step	Reagents	P-bearing phase
1-a	10 ml Na-dithionite solution, bicarbonate buffered (CDB; pH 4, shake for 8 h)	$P_{\text{Fe-ox1}}$ : iron bound to iron(oxyhydr)oxides
1-b	10 ml 1 M Na-acetate solution (pH 4, for 8 h)	$P_{\text{aut}}$ : phosphorus in apatite and carbonate
-	5 ml $\text{MgCl}_2$ (pH 8, for 2 h)	extraction of soluble P after step 1-b, repeated until no P could be extracted
-	5 ml MilliQ water	extraction of soluble P after $\text{MgCl}_2$ wash
1-c	10 ml 10% HCl (shake for 16 h)	$P_{\text{det}}$ : phosphorus bound in crystalline phases (e.g. sheet silicates)
1-d	10 ml Ammonium oxalate solution (shake for 6 h)	$P_{\text{mag}}$ : phosphorus bound as magnetite
-	5 ml $\text{MgCl}_2$ (pH 8, for 2 h)	extraction of soluble P after step 1-d
1-e	10 ml Na-dithionite solution, citrate buffered (CDA; pH 4.5, shake for 2 h)	$P_{\text{Fe-ox2}}$ : iron bound to crystalline iron(oxyhydr)oxides
-	5 ml $\text{MgCl}_2$ (pH 8, for 2 h)	extraction of soluble P after step 1-e
1-f	ashing at 550 °C, 10 ml 10% HCl (shake for 16 h)	$P_{\text{org}}$ : phosphorus bound to organic matter
2	ashing at 550 °C, 5 ml conc. $\text{HNO}_3$ , ~10 ml conc. HF (boiling and evaporating at 120-150 °C to dryness)	$P_{\text{tot}}$ : total iron; including silicates

## 6.2 Carbon and sulfur isotope analysis

Carbonate was removed from the powdered rock samples by dissolution with 2 M HCl. The residues were repeatedly washed with MilliQ water<sup>TM</sup> and dried at 40 °C. The de-carbonated samples were then analyzed for total organic carbon (TOC = C<sub>org</sub>) content and associated carbon isotopic composition using an Elementar Pyrocube elemental analyser linked to an Isoprime mass spectrometer.

The acid washed sample powder was weighed into a tin capsule and combusted at 1150 °C in the presence of pure oxygen (N5.0) injected into a stream of helium (CP grade). Complete oxidation of resulting gases was achieved by passing them through tungstic oxide heated to 1150 °C. Water and excess oxygen were removed from the gas stream by Sicapent and fine copper wires heated to 850 °C respectively. N<sub>2</sub> passes through the system unchecked, whilst CO<sub>2</sub> and SO<sub>2</sub> are removed and reinjected into the gas stream using temperature controlled adsorption-desorption columns. The  $\delta^{13}\text{C}_{\text{org}}$  of the sample is calculated from the integrated mass 44, 45 and 46 signals from the pulse of sample CO<sub>2</sub> compared to that of an independently introduced pulse of reference gas (CP grade). Carbon isotope analyses were calibrated with in-house C4-sucrose and urea standards assigned values of -11.93 ‰ and -46.83 ‰ respectively via calibration with the international standards (assigned values with respect to VPDB in brackets), LSVEC (-46.48 ‰), CH7 (-31.83 ‰), CH6 (-10.45 ‰), and CO-1 (+2.48 ‰). The analytical precision of the carbon isotope measurements was checked with a C-3 internal lab standard and yielded a value of 0.05 ‰ (2SD). TOC values were derived from the combined area of all three mass traces and calibrated using the known weight % C of the C4 sucrose standard. The reproducibility of

these analyses with similar samples from previous runs gives RSDs for in-house standard materials of ~10 %. TOC values were corrected for weight-loss during acid digestion.

The Pyrocube was configured in the same way as described above for carbon isotope analysis.

The  $\delta^{34}\text{S}$  was derived from the integrated mass 64 and 66 signals of the sample gas compared to a pulse of independently introduced reference gas, and was calibrated to the international V-CDT scale using an lab-internal barium sulfate standard derived from seawater (SWS-3) which has been analysed against the international standards (assigned VCDT value in brackets), NBS-127 (+20.30 ‰), NBS-123 (+17.01 ‰), IAEA S-1 (-0.30 ‰) and IAEA S-3 (-32.06 ‰). The analytical precision was checked with an internal suite of reference materials and a barium sulfate standard and yielded a value of 0.9 ‰ (2SD) or better.

### **6.3 Mineralogical analysis**

A subset of samples from both sites was prepared for a mineralogical investigation by mounting rock fragments in an epoxy resin. The mounted samples were subsequently ground, polished and carbon coated. The mineralogical analysis was performed with a Quanta-650F electron microscope from Fisher Thermo Scientific (at Shell Global Solutions International B.V.) was used, which is equipped with a FEG tip for stable electron emission and with two Bruker XFlash EDX detectors, thereby allowing for high count rates. The application: MAPS Mineralogy, records the backscattered electron (BSE) image and the EDX data at high resolution, thereafter the Nanomin TM application translates this data into a detailed mineral map.

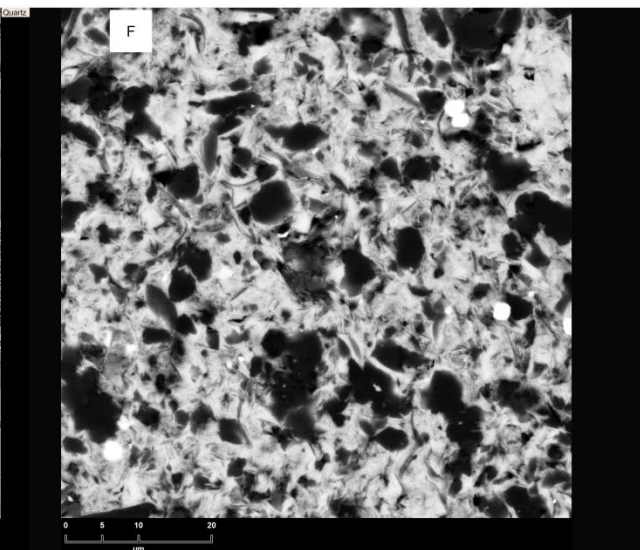
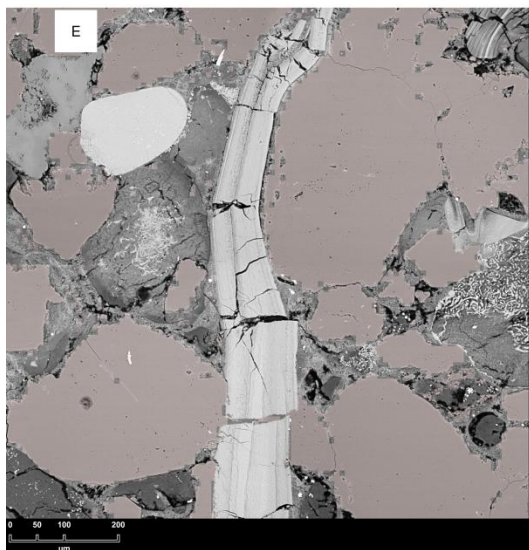
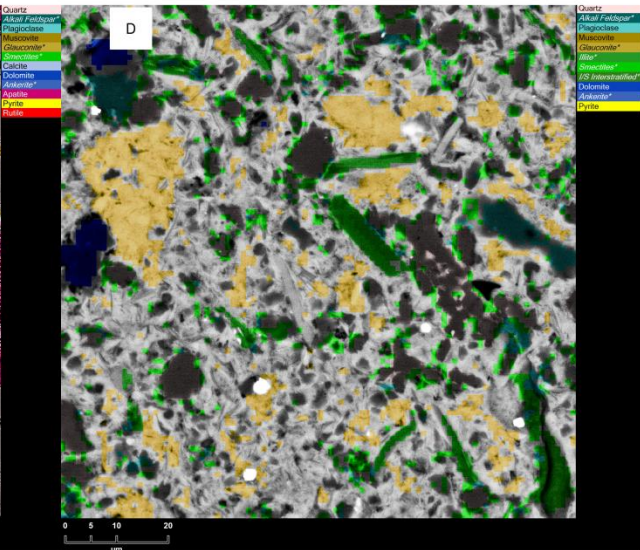
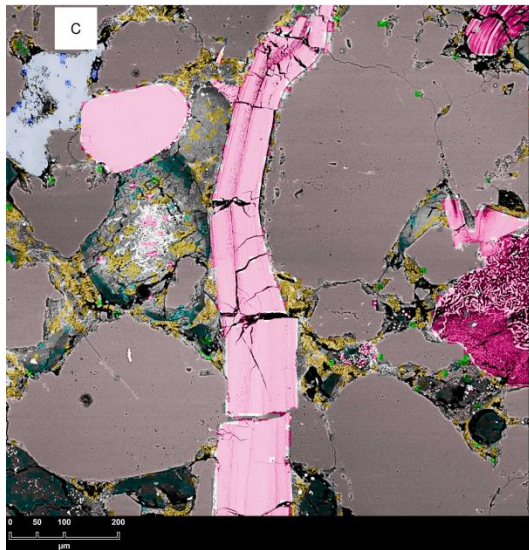
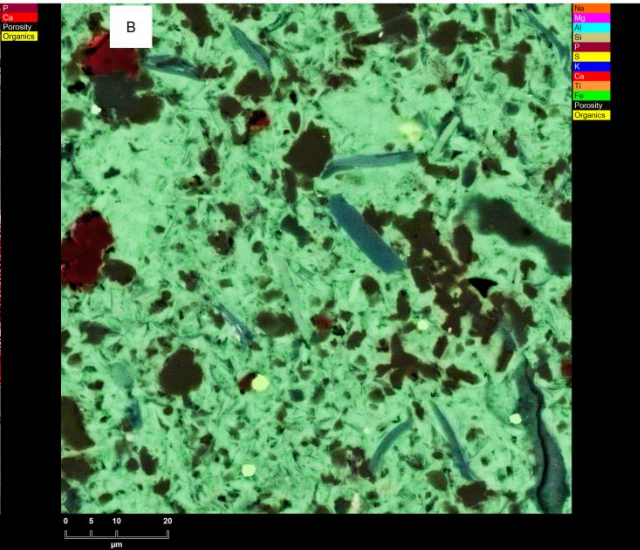
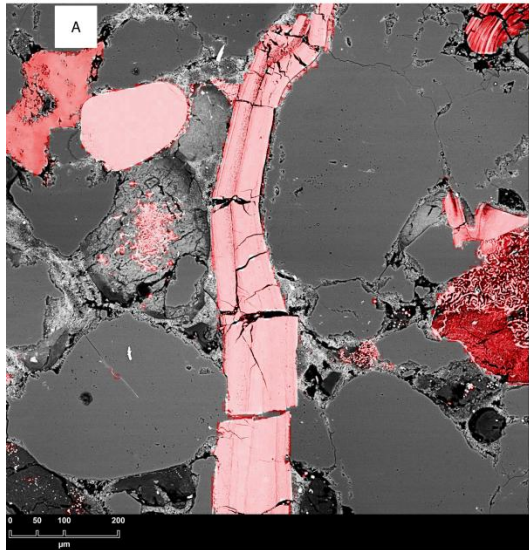


**Figure 3: Microscale mineralogical and elemental variations mapped for A, C, E) Deltadalen at 95.9 m depth, and B, D, F) Festningen 1.6 m above the base of the Vardebukta Formation.** Note, that the fine sand-sized clast of Deltadalen are composed of quartz (E) and apatite shell fragments (C; likely belonging to the inarticulate brachiopods) with porespace occupied by glauconite and authigenic apatite infillings (C). Clasts of Festningen are clay-sized, and, although, P is detected with EDS (B), P bearing minerals could not be identified (D). The mineral assemblage is dominated by dolomite, ankerite and sheet silicates (D, F).

## 7 Supplementary Results and Discussion

### 7.1 Palaeontological results

#### 7.1.1 Body fossils

Benthic macrofaunal communities were investigated at both Festningen and Deltadalen (including Lusitaniadalen): at Festningen benthic fossils were only observed in laminated shales ~8 m above the base of the Vardebukta Formation, which included an assemblage of bivalves including *Claraia kilenensis* and *C. radialis*<sup>48</sup>. At the Deltadalen and Lusitaniadalen sections, the glauconitic sandstones below the mass extinction horizon contain a monospecific assemblage of the inarticulate brachiopod *Lingularia freboldi*, and the first concretionary horizon above the extinction horizon contains an assemblage of *Lingularia* cf. *yini* and abundant sponge spicules<sup>48</sup>. Furthermore, two concretionary horizons at 11.9 and 12.6 m yield a diverse benthic fauna including bivalves, gastropods, microconchids, inarticulate brachiopods, sponges, and foraminifera<sup>15</sup>.

Within this fauna there are a large proportion of larval shells, which reveal the ontogenetic development of the recorded species. The larval stages were studied using an SEM<sup>15</sup> and for many of the bivalve species it was observed that they had a small prodissoconch I and a relatively large prodissoconch II (Supplementary Fig. 4B), which indicates a planktotrophic larval stage<sup>49</sup>. In addition, some of the dominant gastropod larvae, *Warthia* and *Pseudozygolpleuridae*, have also been described as having planktotrophic larvae<sup>50,51</sup>. Extant inarticulate brachiopods, such as *Lingula*, are also observed to have planktotrophic larvae<sup>52,53</sup>, which are morphologically similar to modern planktotrophic inarticulate brachiopods *Lingula anatina* and *Discinisca* (Supplementary Fig. 4B).

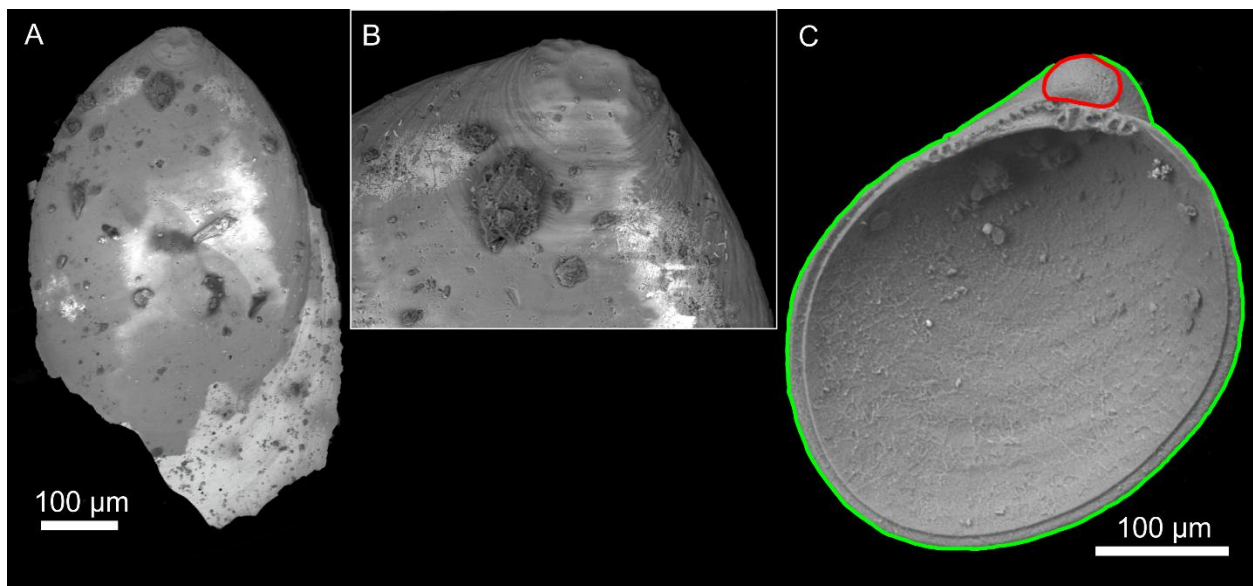


**Figure 4: Early stage larval shell development.** A) the brachiopod *Lingularia*, B) zoomed in on the initial shell formation stages, and C) *Nucinella taylori*, collected from a concretion at 12.6 m above the base of the Vikinghogda Formation. The red outline indicates prodissoconch I and the green outline indicates prodissoconch II.

It has also been shown that the size of the lophophore in Permian–Triassic lingulids can be reconstructed by measuring the size of the lophophoral cavity, i.e., the distance between the anterior adductor on the ventral valve and the anterior obliques on the dorsal valve to the shell margin<sup>54,55</sup>. Supplementary Fig. 5 shows two specimens of lingulid lophophoral cavities measured in this study. These brachiopods have lophophoral cavities significantly larger than is usual for lingulids, which has been related to reduced oxygen availability<sup>54,55</sup>.

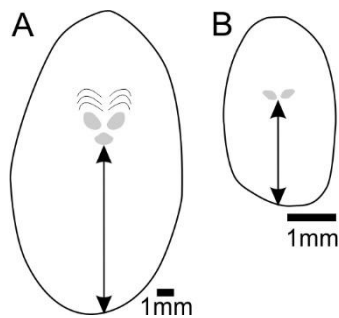


**Figure 5: Outlines of A) *Lingularia freboldi* and B) *L. yini* showing the size of lophophoral cavity (arrow) and the central muscle scars.**

### 7.1.2 Ichnology

**Deltadalen.** The glauconitic sandstones of the Kapp Starostin Formation and the basal part of the Vikinghøgda Formation are highly bioturbated with the bedding completely disturbed and discrete trace fossils are still visible in some places, giving an ichnofabric index (ii)<sup>56</sup> value of 5 (Supplementary Fig. 2). The discrete trace fossils identified in these beds include *Zoophycos*, *Thalassinoides*, and *Rhizocorallium*, which are preserved in full relief. Below the last glauconitic sandstone bed at Deltadalen there is a 20 cm black siltstone bed that is less than 10% bioturbated (ii2). The mudstones that overly the glauconitic sandstones, and represent the post-extinction

strata, do not record any macroscopic bioturbation (ii1), but rare microburrows can be recognised in micro-CT images<sup>4</sup>.

In the nearby Lusitaniadalen section, which is approximately 4.5 km northwest of Deltadalen and records the same lithological succession, a similar ichnofaunal record is recorded. The glauconitic sandstones of the Kapp Starostin and Vikinghøgda formations are completely bioturbated (ii5), and the discrete trace preserved in full relief includes large *Thalassinoides*, *Arenicolites*, *Palaeophycus* and *Skolithos*<sup>16</sup>. The overlying post-extinction mudstones are mostly not bioturbated (ii1), but a few thin horizons are recorded as being disturbed by isolated traces (ii2)<sup>15</sup>. Approximately 8.5 m above the extinction horizon, there is a thin, fine sandstone bed that records small *Planolites*, *Thalassinoides*, *Arenicolites*, and cf. *Lockeia* as convex hyporeliefs. The subsequent sandstones of the Vikinghøgda Formation, which become more abundant up section, are also characterised by similar trace fossils, but also includes *Diplocraterion*, *Arenicolites* and *Skolithos* in full relief, and can be up to 50% disturbed by bioturbation (ii2 to ii4). Furthermore, in the Kapp Starostin Formation below the glauconitic sandstones (from 15 m below the extinction horizon) the succession is characterised by alternations of completely homogenised carbonate mudstone (ii6) overprinted by some discrete trace fossils disturbing between 10 and 50% of the sediment (ii3-4). These discrete trace fossils include *Zoophycos* and cf. *Taenidium* with regularly spaced meniscate backfills, preserved in full relief. These carbonate mudstones alternate with mudstone beds devoid of carbonate, but are between 40 to 80% bioturbated (ii4-5).

**Festningen.** At the Kapp Starostin Formation of Festningen, no primary sedimentary structures remain, and discrete trace fossils are visible at numerous levels, resulting in an ichnofabric index (ii) value of 5 (with the exception of bed Fe 68b = ii4)(Supplementary Fig. 2). Many levels are so

thoroughly bioturbated that individual trace fossils cannot be identified, but we recognize common *Zoophycos* (bed Fe 66-68a and 74-87) as well as *Chondrites*, *Thalassinoides* and *Helminthoidea*, which are preserved in full relief and sometimes pyritized. Diplocraterion can occasionally be seen in concretions. The basal two meters of the Vardebukta Formation contains horizontal, small (1 mm), mud filled burrows (ii4). Laminated strata (ii1) begin at bed Fe 91. A thin, wave-rippled horizon at 92.2 m contains small (1 mm), mud-filled *Arenicolites* burrows (ii2), above which bioturbation is lacking (ii1) for the remainder of the sequence. Thus, the extinction horizon at Festningen is marked by the abrupt loss of large-scale burrows such as *Zoophycos* that are common in pre-extinction strata. In contrast to Deltadalen, small-scale burrowing continues in the basal meters of the post-extinction strata, before petering out a little below the P-T boundary.

## **7.2 Post-depositional alteration of Fe speciation signatures**

By using core material and carefully selecting outcrop material least affected by weathering, we attempted to create geochemical records representative of the primary depositional conditions for both sites. However, modern oxidative weathering may potentially affect reduced Fe-phases sampled in outcrop, such as iron sulfides and ferrous carbonates, which may be oxidized to Fe (oxyhydr)oxides. While such weathering would skew the partitioning of Fe among the different phases, it does not alter the total  $Fe_{HR}$  pool. Furthermore, the appreciable amounts of pyrite found in both outcrop and core materials demonstrate that oxidative weathering was negligible. In the most extreme case, complete oxidation of iron sulfides to iron oxides could create a “false signal” of ferruginous conditions. However, the ferruginous interval of the Festningen locality is rich in magnetite and ferrous carbonates, which precludes the development of a false ferruginous signal (Fig. 2).

Although the ‘poorly reactive sheet silicate Fe’ ( $\text{Fe}_{\text{PRS}}$ ) is generally of less importance in establishing ancient redox conditions, it is a frequently observed phenomenon that  $\text{Fe}_{\text{HR}}$  is channelled into  $\text{Fe}_{\text{PRS}}$  pool in ancient rock samples, particularly where TOC is abundant and the supply of  $\text{Fe}_{\text{HR}}$  minerals overwhelms the availability of sulfate to fuel enough sulfide production during early diagenesis to pyritise the majority of the  $\text{Fe}_{\text{HR}}$  pool supplied to the sediment<sup>57,58</sup>. Such conversion of  $\text{Fe}_{\text{HR}}$  is associated with the post-depositional formation of iron-containing phyllosilicate minerals (e.g. glauconite as present at both sites), thereby transforming a fraction of the  $\text{Fe}_{\text{HR}}$  to these less-reactive phases. This option can be tested by evaluating  $\text{Fe}_{\text{tot}}/\text{Al}$  (Supplementary Fig. 6), whereby enrichments over the average shale value are still preserved irrespective of diagenetically-driven transformations between different Fe pools<sup>57-59</sup>. This approach allowed us to define a primary baseline  $\text{Fe}_{\text{PRS}}/\text{Fe}_{\text{tot}}$  ratio for each site, which represents the ratio at times when a high degree of glauconite formation was not apparent (Supplementary Fig. 6). Using this approach, we were able to apply a correction to samples with high glauconite (which is sourced from the original  $\text{Fe}_{\text{HR}}$  pool), to estimate the original  $\text{Fe}_{\text{HR}}$  concentration of the deposited sediment (thereby giving corrected Fe speciation ratios denoted by  $\text{Fe}_{\text{HR}}/\text{Fe}_{\text{tot}}^*$  and  $\text{Fe}_{\text{py}}/\text{Fe}_{\text{HR}}^*$ ), whereby  $\text{excess Fe}_{\text{PRS}} = (\text{measured Fe}_{\text{PRS}}/\text{Fe}_{\text{tot}} - \text{baseline Fe}_{\text{PRS}}/\text{Fe}_{\text{tot}}) \times \text{Fe}_{\text{tot}}$  if  $\text{measured Fe}_{\text{PRS}}/\text{Fe}_{\text{tot}} > \text{baseline Fe}_{\text{PRS}}/\text{Fe}_{\text{tot}}$ <sup>60</sup>.

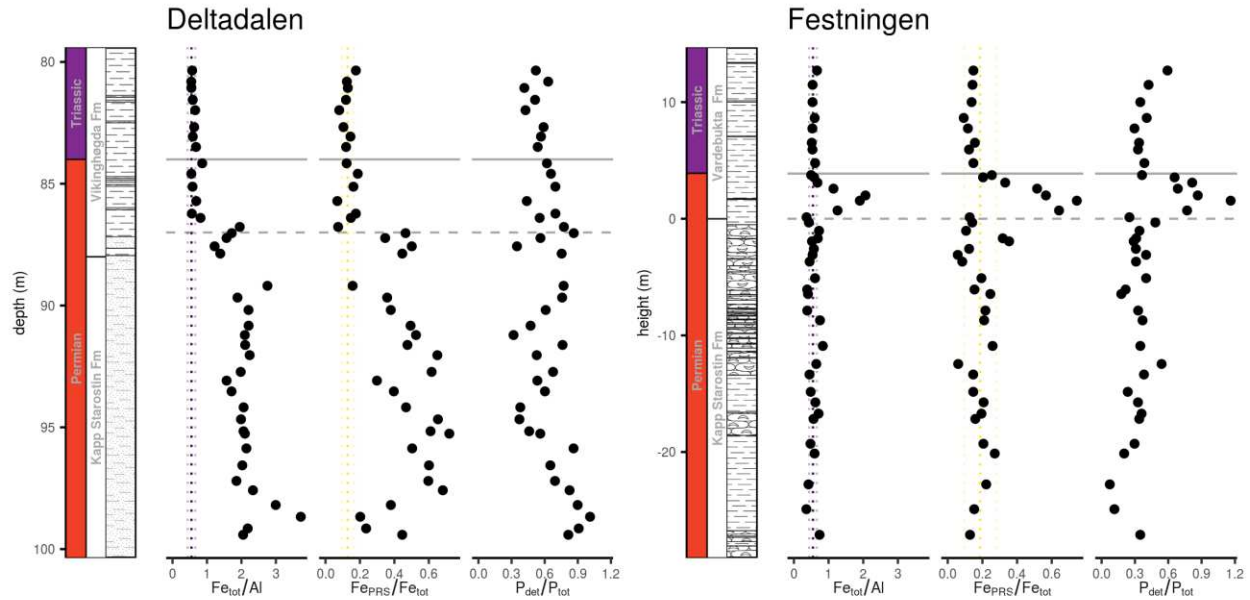


**Figure 6: Stratigraphic plots of  $Fe_{tot}/Al$ ,  $Fe_{PRS}/Fe_{tot}$  and  $P_{det}/P_{tot}$  of the Festningen site and Deltadalen core.** The static boundary for the  $Fe_{tot}/Al$  (mass ratio) represents the average shale value<sup>61,62</sup>. On the  $Fe_{PRS}/Fe_{tot}$  the dashed lines represent the site-specific background values (Deltadalen:  $0.13 \pm 0.04$  and Festningen:  $0.19 \pm 0.09$ ) and their respective uncertainty (SD). Horizontal dashed grey line: extinction event; solid grey line: Permian–Triassic boundary.

### 7.3 Post-depositional alteration of P speciation signatures

Post-depositional processes may also impact on the speciation of P phases. Indeed, early diagenetic phase transformations are a crucial aspect of sedimentary P retention that provide insight into redox controlled P cycling (see main text). However, there is also the potential for late stage diagenetic recrystallization of original authigenic apatite, leading to its extraction (and hence over-estimation) as part of the  $P_{det}$  pool. It is evident from Supplementary Fig. 6 that relative enrichments in  $P_{det}$  occur at some horizons, but these horizons specifically coincide with enrichments in glauconite, suggesting that the sediments have not been universally affected by

significant recrystallisation of authigenic P. The horizons that contain high  $P_{\text{det}}$  are also enriched in total P, and the speciation characteristics imply that Fe (oxyhydr)oxide minerals were likely a primary source of this P to the sediment (Supplementary Fig. 7). Given these considerations, it appears highly likely that after delivery to the sediment in association with Fe (oxyhydr)oxide minerals, the re-working of these minerals to glauconite resulted in sequestration of a fraction of released  $P_{\text{Fe}}$  in association with glauconite (and possibly also some recrystallization of  $P_{\text{aut}}$  to apatite). Fe(III)-rich phyllosilicates and clays (e.g., mica and smectite groups, among which glauconite) are known to have a phosphate adsorption capacity, which relates to constituent Fe(III) within interlayer spaces and iron-oxide coating of the particle surface<sup>46,63</sup>. These inorganic P phases are likely to have been liberated during step 1-c of the sequential extraction protocol (Supplementary Table 3)<sup>46</sup>.

Therefore, the high P content of the glauconite-rich horizons is consistent with an elevated weathering influx of reactive P from the continents, combined with an effective retention mechanism in the sediment, rather than high primary  $P_{\text{det}}$  fluxes. However, even if our  $P_{\text{det}}$  measurements are representative of primary  $P_{\text{det}}$  inputs to the sediment, the enrichments in  $P_{\text{Fe}}$  and  $P_{\text{aut}}$  observed across these horizons still supports a high weathering influx of reactive P. Furthermore, our conclusions in terms of sedimentary P recycling are unaffected by possible transfer of reactive P to  $P_{\text{det}}$  in glauconite-rich horizons, since our calculated  $C_{\text{org}}/P_{\text{reac}}$  ratios would be even lower than the Redfield ratio if original  $P_{\text{reac}}$  contents were underestimated (see main text). Phosphatic shell fragments occur in the glauconite-rich beds of Deltadalen, but are absent from the glauconite-rich unit of Festningen (Supplementary Fig. 3), so while phosphatic shell fragments likely comprises a small portion of the  $P_{\text{aut}}$  pool, and might have skewed  $C_{\text{org}}/P_{\text{reac}}$  ratios again to higher values, this source of P can be discounted for Festningen. Hence,

CFA and Fe(III)-rich sheet silicates (as  $P_{\text{aut}}$  and  $P_{\text{det}}$ ) seems to be the quantitatively most important sinks for P for this sedimentary environment.

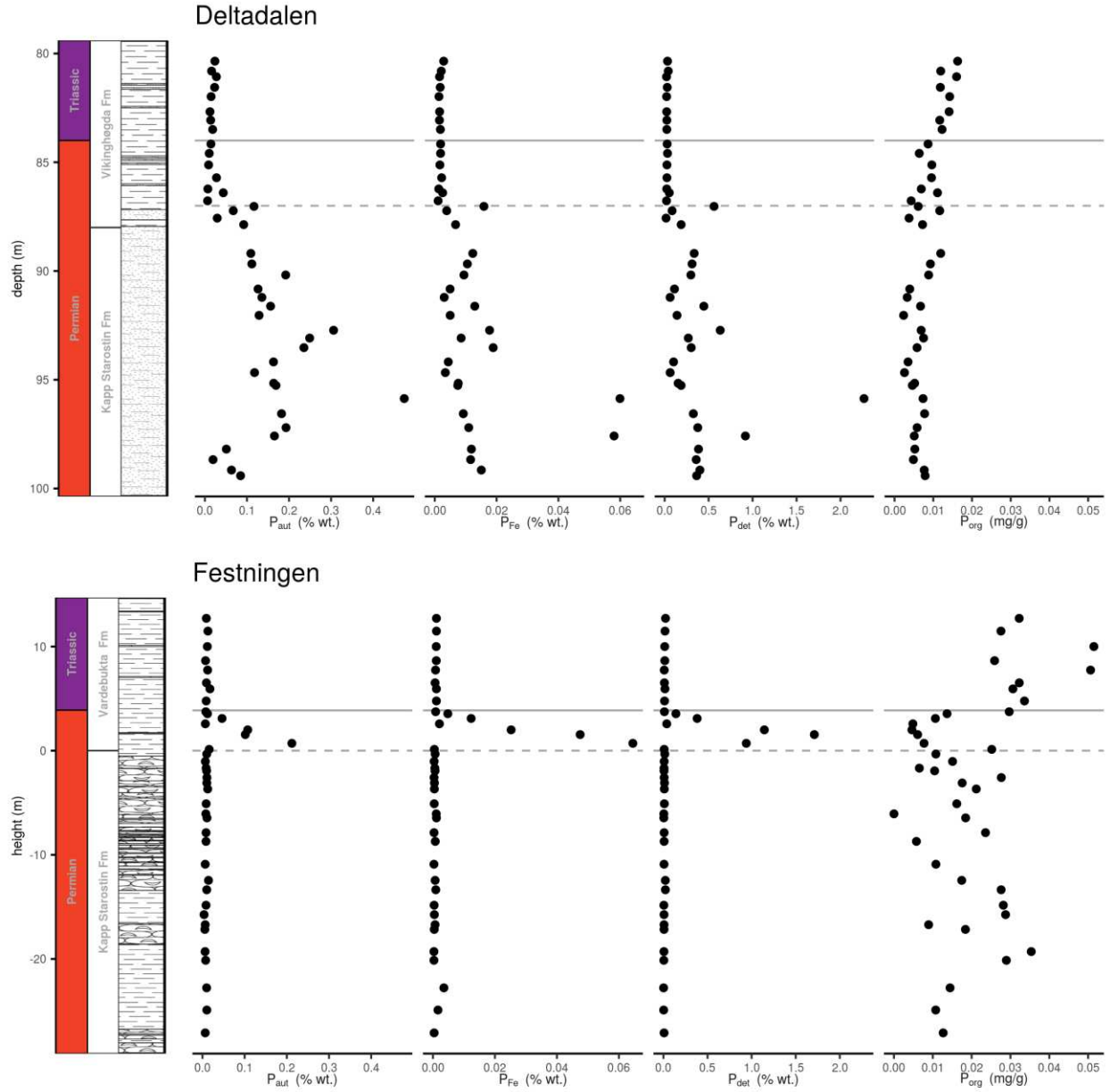


**Figure 7: Stratigraphic plots of P phases of Festningen and Deltadalen.** Note that  $P_{\text{mag}}$  and  $P_{\text{Fe-ox}}$  have been lumped in  $P_{\text{Fe}}$ . Horizontal dashed grey line: extinction event; solid grey line: Permian–Triassic boundary.

## 8 References

1. Dallmann, W. *et al.* Upper Palaeozoic Lithostratigraphy. in *Lithostratigraphic lexicon of svalbard* (ed. Dallmann, W.) 25–126 (Norsk Polarinstitut, 1999).
2. Harland, W. *The geology of Svalbard*. 521 (Geological Society Memoir No.17, 1997).
3. Grasby, S. E. *et al.* Progressive environmental deterioration in northwestern Pangea leading to the latest Permian extinction. *Bull. Geol. Soc. Am.* **127**, 1331–1347 (2015).
4. Zuchuat, V. *et al.* A new high-resolution stratigraphic and palaeoenvironmental record spanning the End-Permian Mass Extinction and its aftermath in central Spitsbergen, Svalbard. *Palaeogeogr. Palaeoclimatol. Palaeoecol.* 109732 (2020)  
doi:[10.1016/j.palaeo.2020.109732](https://doi.org/10.1016/j.palaeo.2020.109732).
5. Mørk, A. *et al.* The type section of the Vikinghøgda Formation: a new Lower Triassic unit in central and eastern Svalbard. *Polar Res.* **18**, 51–82 (1999).
6. Johansson, L., Zahirovic, S. & Müller, R. D. The interplay between the eruption and weathering of Large Igneous Provinces and the deep-time carbon cycle. *Geophys. Res. Lett.* 5380–5389 (2018).
7. Matthews, K. J. *et al.* Global plate boundary evolution and kinematics since the late Paleozoic. *Global Planet. Change* **146**, 226–250 (2016).
8. Seton, M. *et al.* Global continental and ocean basin reconstructions since 200Ma. *Earth-sci. Rev.* **113**, 212–270 (2012).

9. Blomeier, D., Dustira, A. M., Forke, H. & Scheibner, C. Facies analysis and depositional environments of a storm-dominated, temperate to cold, mixed siliceous–carbonate ramp: the Permian Kapp Starostin Formation in NE Svalbard. *Norw. J. Geol.* **93**, 75–93 (2013).
10. Dustira, A. M. *et al.* Gradual onset of anoxia across the Permian-Triassic Boundary in Svalbard, Norway. *Palaeogeogr. Palaeoclimatol. Palaeoecol.* **374**, 303–313 (2013).
11. Bond, D. P. G. *et al.* An abrupt extinction in the Middle Permian (Capitanian) of the Boreal Realm (Spitsbergen) and its link to anoxia and acidification. *Bull. Geol. Soc. Am.* **127**, 1411–1421 (2015).
12. Bond, D. P. *et al.* Sequence stratigraphy, basin morphology and sea-level history for the Permian Kapp Starostin Formation of Svalbard, Norway. *Geol. Mag.* **155**, 1023–1039 (2017).
13. Mørk, A. *et al.* Mesozoic Lithostratigraphy. in *Lithostratigraphic lexicon of svalbard* (ed. Dallmann, W.) 127–214 (Norsk Polarinstitut, 1999).
14. Wignall, P. B. *et al.* Ultra-shallow-marine anoxia in an Early Triassic shallow-marine clastic ramp (Spitsbergen) and the suppression of benthic radiation. *Geol. Mag.* **153**, 316–331 (2016).
15. Foster, W. J., Danise, S. & Twitchett, R. J. A silicified Early Triassic marine assemblage from Svalbard. *J. Syst. Palaeontol.* **15**, 851–877 (2017).
16. Nabbefeld, B. *et al.* Significance of  $\delta D_{\text{kerogen}}$ ,  $\delta^{13}C_{\text{kerogen}}$  and  $\delta^{34}S_{\text{pyrite}}$  from several Permian/Triassic (P/Tr) sections. *Earth Planet. Sc. Lett.* **295**, 21–29 (2010).

17. Wignall, P. B. & Twitchett, R. J. Oceanic anoxia and the End Permian mass extinction. *Science* **272**, 1155–1158 (1996).
18. Arthur, M. A., Dean, W. E. & Claypool, G. E. Anomalous  $^{13}\text{C}$  enrichment in modern marine organic carbon. *Nature* **318**, 216–218 (1985).
19. Cao, C. *et al.* Biogeochemical evidence for euxinic oceans and ecological disturbance presaging the end-Permian mass extinction event. *Earth Planet. Sc. Lett.* **281**, 188–201 (2009).
20. Nakrem, H. A., Nilsson, I. & Mangerud, G. Permian Biostratigraphy of Svalbard (Arctic Norway)—A Review. *Int. Geol. Rev.* **34**, 933–959 (1992).
21. Nakrem, H. A. *et al.* Triassic conodonts from Svalbard and their Boreal correlations. in *Polar research* vol. 27 523–539 (Routledge, 2008).
22. Yin, H., Zhang, K., Tong, J., Yang, Z. & Wu, S. The global stratotype section and point (GSSP) of the Permian-Triassic boundary. *Episodes* **24**, 102–114 (2001).
23. Korte, C. & Kozur, H. W. Carbon-isotope stratigraphy across the Permian–Triassic boundary: A review. *J. Asian Earth Sci.* **39**, 215–235 (2010).
24. Wignall, P. B., Morante, R. & Newton, R. The Permo-Triassic transition in Spitsbergen:  $\delta^{13}\text{C}_{\text{org}}$  chemostratigraphy, Fe and S geochemistry, facies, fauna and trace fossils. *Geol. Mag.* **135**, 47–62 (1998).
25. Xie, Y. *Knitr: A general-purpose package for dynamic report generation in r.* (2020).
26. Xie, Y. *Dynamic documents with R and knitr.* (Chapman; Hall/CRC, 2015).

27. Xie, Y. Knitr: A comprehensive tool for reproducible research in R. in *Implementing reproducible computational research* (eds. Stodden, V., Leisch, F. & Peng, R. D.) (Chapman; Hall/CRC, 2014).
28. R Core Team. *R: A language and environment for statistical computing*. (R Foundation for Statistical Computing, 2020).
29. Wickham, H. *tidyverse: Easily Install and Load the 'Tidyverse'*. (2017).
30. Wickham, H. & Pedersen, T. L. *Gtable: Arrange 'grobs' in tables*. (2019).
31. Urbanek, S. *Png: Read and write png images*. (2013).
32. Auguie, B. *GridExtra: Miscellaneous functions for "grid" graphics*. (2017).
33. Wickham, H. & Bryan, J. *Readxl: Read excel files*. (2019).
34. Francois, R. *bibtex: Bibtex Parser*. (2017).
35. Pebesma, E. J. & Bivand, R. S. Classes and methods for spatial data in R. *R News* **5**, 9–13 (2005).
36. Bivand, R. S., Pebesma, E. & Gomez-Rubio, V. *Applied spatial data analysis with R, second edition*. (Springer, NY, 2013).
37. Bivand, R., Keitt, T. & Rowlingson, B. *Rgdal: Bindings for the 'geospatial' data abstraction library*. (2019).
38. Bivand, R. & Rundel, C. *Rgeos: Interface to geometry engine - open source ('geos')*. (2019).
39. Sarkar, D. *Lattice: Multivariate data visualization with r*. (Springer, 2008).
40. Soetaert, K. & Petzoldt, T. *marelac: Tools for Aquatic Sciences*. (2018).

41. Poulton, S. W. & Canfield, D. E. Development of a sequential extraction procedure for iron: Implications for iron partitioning in continentally derived particulates. *Chem. Geol.* **214**, 209–221 (2005).
42. Canfield, D. E., Raiswell, R., Westrich, J. T., Reaves, C. M. & Berner, R. a. The use of chromium reduction in the analysis of reduced inorganic sulfur in sediments and shales. *Chem. Geol.* **54**, 149–155 (1986).
43. Raiswell, R., Canfield, D. E. & Berner, R. A. A comparison of iron extraction methods for the determination of degree of pyritisation and the recognition of iron-limited pyrite formation. *Chem. Geol.* **111**, 101–110 (1994).
44. Raiswell, R. & Canfield, D. E. Rates of reaction between silicate iron and dissolved sulfide in Peru Margin sediments. *Geochim. Cosmochim. Ac.* **60**, 2777–2787 (1996).
45. Raiswell, R. & Canfield, D. E. Sources of iron for pyrite formation in marine sediments. *Am. J. Sci.* **298**, 219–245 (1998).
46. Ruttenberg, K. C. Development of a sequential extraction method for different forms of phosphorus in marine sediments. *Limnol. Oceanogr.* **37**, 1460–1482 (1992).
47. Thompson, J. *et al.* Development of a modified SEDEX phosphorus speciation method for ancient rocks and modern iron-rich sediments. *Chem. Geol.* **524**, 383–393 (2019).
48. Foster, W. Palaeoecology of the late Permian mass extinction and subsequent recovery. (University of Plymouth, 2015).

49. Hautmann, M. & Nützel, A. First record of a heterodont bivalve (mollusca) from the early triassic: Palaeoecological significance and implications for the 'lazarus problem'. *Palaeontology* **48**, 1131–1138 (2005).
50. Frýda, J. Higher classification of Paleozoic gastropods inferred from their early shell ontogeny. *J. Cz. Geol. Soc.* **44**, 137–154 (1999).
51. Maps, R. H. & Nützel, A. Late Palaeozoic mollusc reproduction: Cephalopod egg-laying behavior and gastropod larval palaeobiology. *Lethaia* **42**, 341–356 (2009).
52. Yatsu, N. On the development of *Lingula anatina*. *J. Coll. Sci. Imp. Univ. Tokyo* **17**, 1–112 (1902).
53. Ashworth, J. On the larvae of *Lingula* and *Pelagodiscus* (*Discinisca*). *Trans. R. Soc. Edinb.* **51**, 45–69 (1915).
54. Peng, Y. & Shi, G. R. New Early Triassic *Lingulidae* (Brachiopoda) genera and species from South China. *Alcheringa* **32**, 149–170 (2008).
55. Posenato, R., Holmer, L. E. & Prinoth, H. Adaptive strategies and environmental significance of lingulid brachiopods across the late Permian extinction. *Palaeogeogr. Palaeoclimatol. Palaeoecol.* **399**, 373–384 (2014).
56. Droser, M. L. & Bottjer, D. J. A semiquantitative field classification of ichnofabric. *J. Sediment. Res.* **56**, 558–559 (1986).
57. Poulton, S. W., Fralick, P. W. & Canfield, D. E. Spatial variability in oceanic redox structure 1.8 billion years ago. *Nat. Geosci.* **3**, 486–490 (2010).

58. Poulton, S. W. & Canfield, D. E. Ferruginous conditions: A dominant feature of the ocean through Earth's history. *Elements* **7**, 107–112 (2011).
59. Lyons, T. W. & Severmann, S. A critical look at iron paleoredox proxies: New insights from modern euxinic marine basins. *Geochim. Cosmochim. Ac.* **70**, 5698–5722 (2006).
60. Doyle, K. A., Poulton, S. W., Newton, R. J., Podkovyrov, V. N. & Bekker, A. Shallow water anoxia in the Mesoproterozoic ocean: Evidence from the Bashkir Meganticlinorium, Southern Urals. *Precambrian Res.* **317**, 196–210 (2018).
61. Wedepohl, K. H. The composition of the upper earth's crust and the natural cycles of selected metals. Metals in natural raw materials. Natural Resources. in *Metals and their compounds in the environment* (ed. Merian, E.) 3–17 (Verlag Chemie, 1991).
62. Clarkson, M. O., Poulton, S. W., Guilbaud, R. & Wood, R. a. Assessing the utility of Fe/Al and Fe-speciation to record water column redox conditions in carbonate-rich sediments. *Chem. Geol.* **382**, 111–122 (2014).
63. Borgnino, L., Avena, M. & De Pauli, C. Synthesis and characterization of Fe(III)-montmorillonites for phosphate adsorption. *Colloid. Surface. A.* **341**, 46–52 (2009).